Supporting Information

Enhancing Oxygen Adsorption Capabilities in Li-O_2 Battery Cathodes through Solid Perfluorocarbons

Moran Balaish[†,*] *and Yair Ein-Eli* [†,††,*]

[†]The Grand Technion Energy Program, Technion- Israel Institute of Technology, Haifa 32000, Israel.

[††]Department of Materials Science and Engineering, Technion- Israel Institute of Technology, Haifa 32000, Israel.

* Corresponding authors E-mail: moran.bala@gmail.com, eineli@technion.ac.il

Contents

1. Electrochemical cells

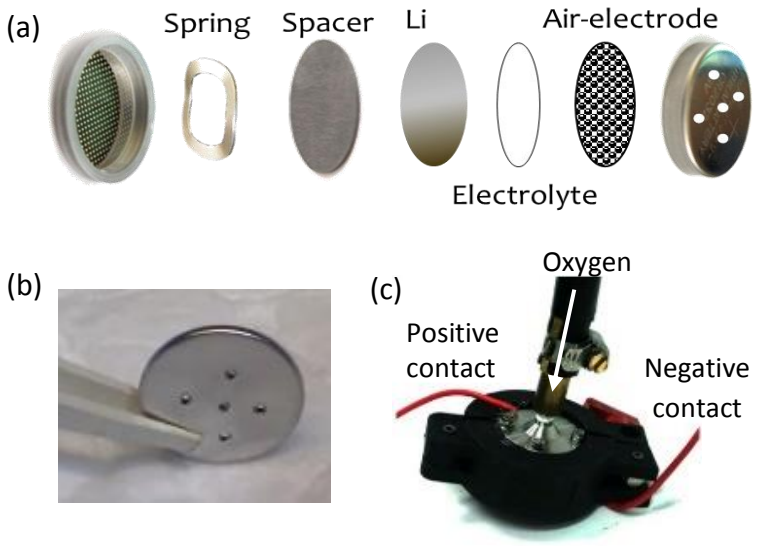

Figure S1. (a) A schematic representation of a modified 2-electrode coin-cell configuration. The cells were constituted from a negative case, spring, spacer, lithium metal (anode), and either an electrolyte-soaked PP Celgard separator or a solid polymer electrolyte, a carbon-based air-cathode and a modified positive case with 5-evenly dispersed holes. (b) An image of an assembled coin-cell configuration. (c) An image of a lab-scale battery compartment constructed in order to prevent any moisture, nitrogen and/or carbon dioxide contamination.[1]

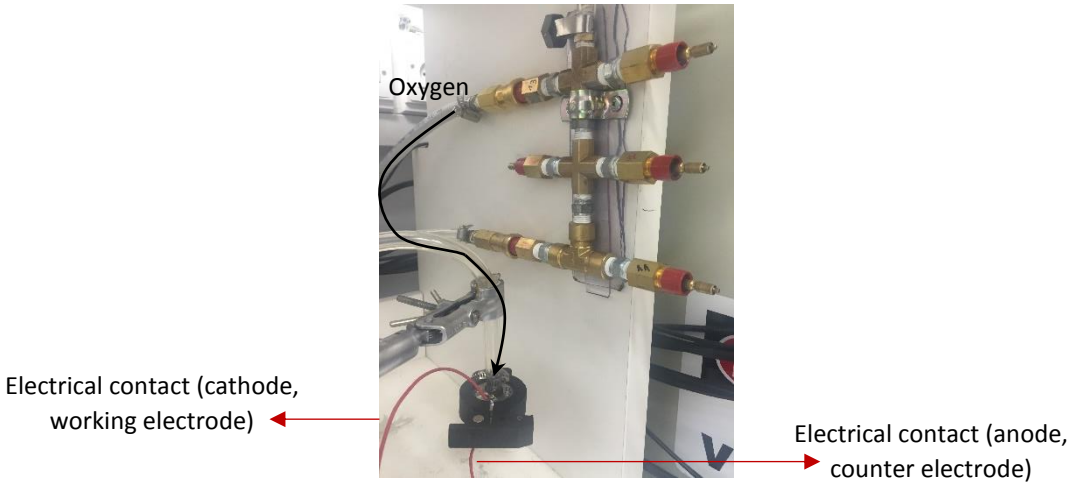

Figure S2. An image of stainless steel compartment connected to a 1 atm oxygen gas-line. The two electrical contacts (shown here as red wires) were connected to a battery cycler for galvanostatic experiments. [1]

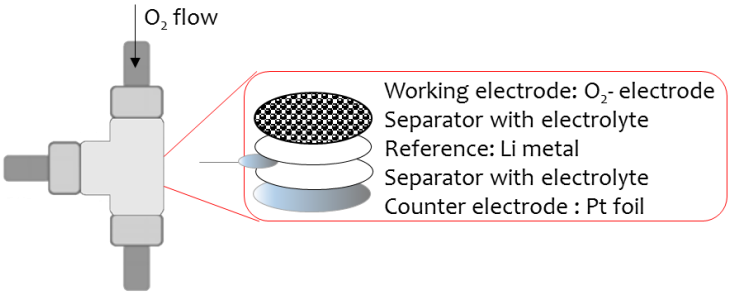

Figure S3. A schematic representation of a three electrode T-shaped cell (T-cell) configuration. The cell was constituted from platinum foil (counter electrode), and either an electrolyte-soaked PP Celgard separator or a solid polymer electrolyte and a carbon-based air-cathode (working electrode). The electrical contacts of the reference and counter electrodes were stainless steel rods, while for the working electrode, a hollow stainless steel rod was used in order to allow oxygen flow into the cell. [1]

2 Experimental Setup for Washburn capillary rise method

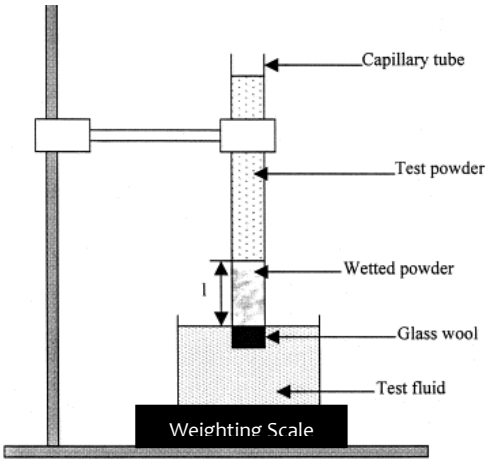

Figure S4. Experimental setup for capillary rise (modified from reference [2])

3 XRD Characterization of A2 and A4 Electrodes

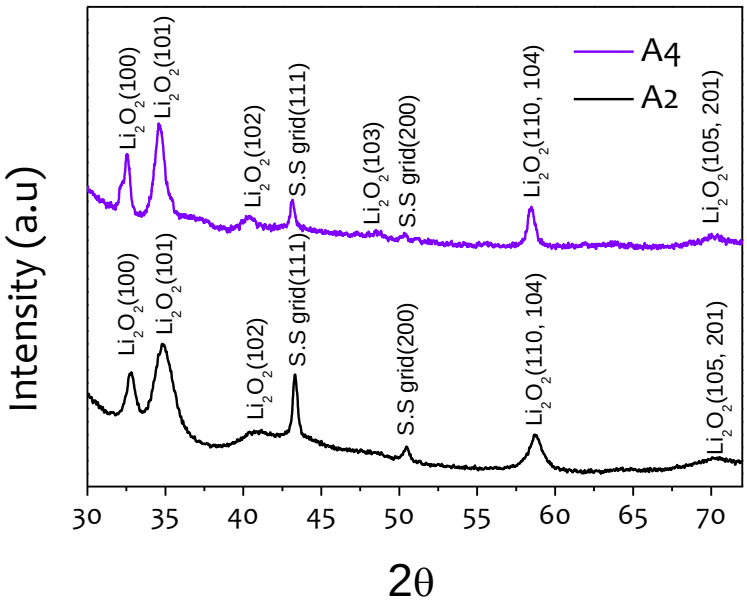

Figure S5. The corresponding XRD patterns of A2 and A4 electrodes after discharged at 0.1 mA cm^{-2}.

4 Surface Characterization of A2 Electrode

4.1 HRSEM and XRD of pristine A2 electrode

XRD spectrum (**Figure S6**(a)) indicated low degree of graphite crystallinity (2θ=25.37˚) in addition to peaks at 2θ=43.44, 50.66, and 74.57˚ corresponding to presence of stainless steel, i.e. current collector, as also indicated from EDS analysis (**Figure S6**(b)). HRSEM images of pristine A2 electrodes are provided in **Figure S6**(c).

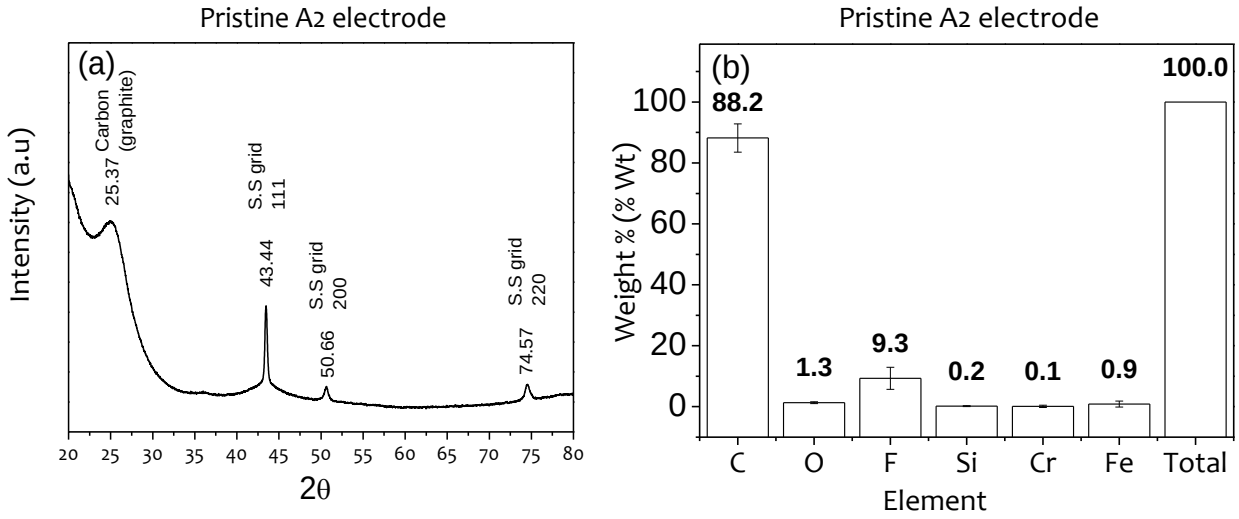

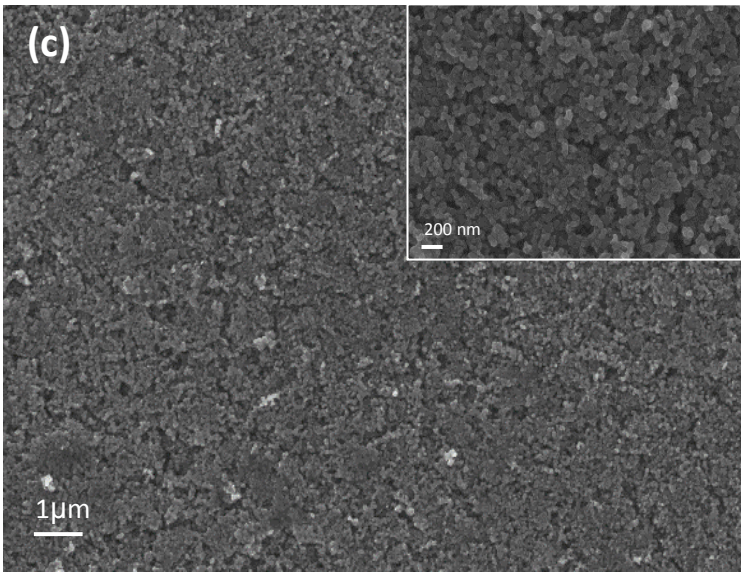

Figure S6. (a) Powder X-ray diffraction and (b) EDS analysis of pristine A2 air-electrode and (c) HRSEM images of pristine A2 air-electrode. (Inset: higher magnification).

4.2 N_2 adsorption/desorption isotherm of A2 electrode

The extent of nitrogen sorption, i.e. the adsorption/desorption isotherms, on A2 powder at different relative pressures are presented in **Figure S7**. The mild increase in adsorbed volume at low relative pressures up to $P/P_0 = 0.2$, followed by the long linear part observed over a wide range of relative pressures and the sharp increase at high relative pressures $P/P_0 > 0.9$, indicate a type IV isotherm for the A2 sample.

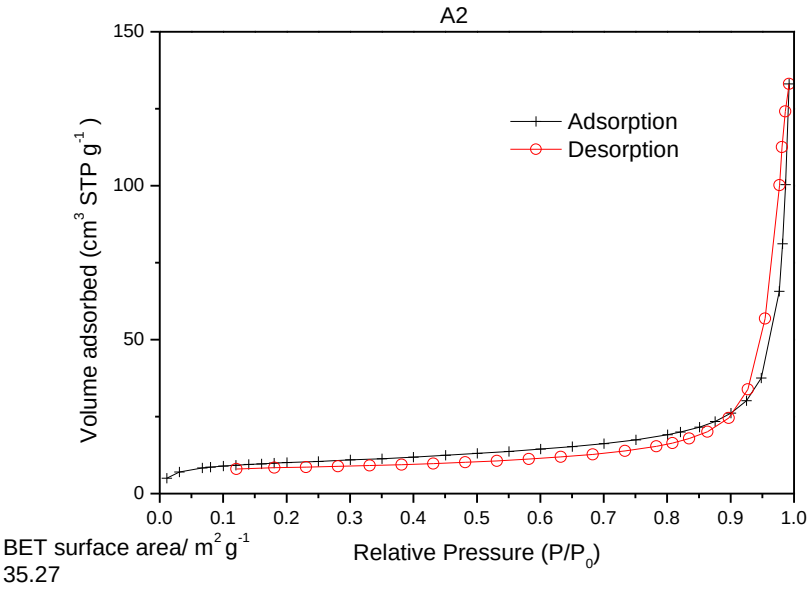

Figure S7. Adsorption/desorption isotherm of N_2 on A2 air-electrode carbon.

The relatively long linear part observed in the adsorption/desorption isotherm of A2, i.e. the 'plateau' in the adsorption isotherm, represents the completion of the monolayer and thus provide the determination of the monolayer capacity. Type IV isotherm is characteristic of a mesoporous structure also manifested in the presence of an hysteresis loop carefully classified as type A[3]. Near the first point of inflection, at relatively low relative pressure (~0.2), the first monolayer is completed, following which adsorption occurs in successive layers. Unlike type I isotherm, limited to the completion of a simple monolayer, type IV isotherm do not exhibit a saturation limit but rather an indefinite multi-layer formation manifested in the sharp increase in adsorbed volume observed at high relative pressures. The steep increase in adsorbed amount at pressures approaching the saturation pressure, as well as the existence of hysteresis, imply that consider fraction of the surface arises from pores which are on the mesopore scale, and possibly on the micropore scale as well. Carbon blacks exhibits different types of isotherms ranging from type II to type IV depending on their specific surface area and degree of mesoporosity.[4,5] The A2 sample, which is on the scale of low surface area carbon black, and exhibited type IV isotherm is predicted to show low degree of mesoporosity.

4.3 Adapting/Processing Adsorption/Desorption Isotherm Data via Different Adsorption Models

4.3.1 Theoretical Background

4.3.1.1 Langmuir

Langmuir provides a means of determining surface area based on a monolayer coverage of the solid surface by the adsorptive. Using a kinetic approach,[6] Langmuir was able to describe an adsorbate-adsorbent system where the adsorbate coverage was limited to a monomolecular layer (Type I isotherm).[6–8] This approach is mostly suited for chemisorption, nevertheless is readily extended to describe physical adsorption of pore filling of micropores. The Langmuir adsorption theory assumes the adsorbate gas (G) behaves as an ideal gas and is in a dynamic equilibrium with a bonded (chemical adsorption) or tightly held (physical adsorption) species on surface (S) sites (chemical adsorption) or surface (physical adsorption)[6–8]

(S1) $$G + S \square \quad G - S \ (Adsorbed\ complex)$$

Therefore, by a simple equilibrium calculation one gets

(S2) $$K_{ads} \cdot (P/P_0) \cdot (1 - q/q_m) = K_{des} \cdot q/q_m$$

Where q, q_m are the capacity and monolayer capacity of the adsorbed gas, P/P_0 is the relative pressure and K_{ads}, K_{des} are the rate of adsorption and desorption, respectively. On linearization, the equation becomes

(S3) $$\frac{P/P_0}{q} = \frac{1}{b \cdot q_m} + \frac{P/P_0}{q_m}$$

Where $b = \frac{K_{ads}}{K_{des}}$ and q_m are treated as empirical constants which can be derived from the slope and Y-intercept of the $\frac{P/P_0}{q}$ versus P/P_0 plot. Having established q_m, the sample surface area, S_t, can then be calculated from Equation (S4):

(S4) $$S_t = \frac{q_m \cdot N_{AV} \cdot A_{cs}}{M_w}$$

Here N_A is Avogadro's number, M_W is nitrogen's molecular weight and A_{CS} is the cross-sectional area of a nitrogen molecule taken as 0.162 nm^2.

4.3.1.2 BET

The Brunauer, Emmet, ands Teller (BET)[9] theory, which is the multi-layer extension of Langmuir's[7] monolayer description of adsorption, although based on an over-simplified model, allows us to determine the specific surface area of a porous material by physical adsorption of a gas on the external and internal surfaces of the solid and by calculating the number of molecules (with a known cross section) required for the creation of a monolayer. The determination of the specific surface area according to the BET method is derived under the assumptions of a multiple layer adsorption on a homogeneous surface, adsorption can be done before the complete filling of the lower levels, and no lateral interactions between molecules (making the molar adsorption energy within one layer constant but differ from that of other layer).

The specific surface area can be calculated after the monolayer capacity, q_m, has been determined, via:

(S5) $$S_{BET} = \frac{q_m \rho_{STP}^{Vap} N_A A_{CS}}{M_W(N_2)}$$

Here ρ_{STP}^{Vap} is the density of nitrogen vapor at standard temperature and pressure (STP), N_A is Avogadro's constant, $M_W(N_2)$ is nitrogen's molar mass and A_{CS} is the cross-sectional area of a nitrogen molecule taken as 0.162 nm^2. In order to calculate the specific surface area, the monolayer capacity, q_m, is to be determined. By plotting the linearized form of the BET equation[10]

(S6) $$\frac{(P/P_0)}{q(1-(P/P_0))} = a + b(P/P_0)$$

That is, plotting the left hand side of Equation (S6) versus relative pressure P/P_0 and obtaining the Y-intercept, a, and the slope, b, in order to back-calculate BET *C*-parameter and monolayer capacity, q_m, via[10]

(S7) $$q_m = \left(\frac{1}{a+b}\right);\ C = \left(\frac{a+b}{a}\right)$$

The BET *C*-parameter is a dimensionless parameter calculated as the ratio between the adsorption constants of the first and second and further layers, often approximated by[10,11]

(S8) $$C \approx \exp\left(\frac{E_1 - E_2}{RT}\right)$$

Where E_1 and E_2 are the molar adsorption energy for the first layer and for the second and further layers, respectively.

4.3.1.3 BJH

The BJH[12] technique is commonly applies to determine the pore size distribution for mesopore materials based on the Kelvin equation and modified to include multilayer adsorption. The Kelvin equation relates the equilibrium vapor pressure of a liquid on a curved surface, such as a cylindrical pore (*P*), to the equilibrium pressure of the same liquid on a planner surface (P_0). For nitrogen adsorption at 77K, the Kelvin radius at which condensation occurs can be written as

(S9) $$r_K = \frac{4.15}{\log(P_0 / P)}$$

Two separate consequent contributions determine the total amount of adsorbate: the adsorption of gas on the walls of all pores with a radius larger than the Kelvin radius (r_K), $r > r_K(P/P_0)$, and condensation of gas in pores with radius smaller than the Kelvin radius $r \le r_K(P/P_0)$, where the pores are filled by condensation rather than by the prolonged layer formation. By evaluating the difference in loading between two consecutive data points, a point at saturation conditions and an adjacent data point at lower relative pressure, the incremental pore volume or surface for the largest pore in the absorbent can be determined. From such an approach the pore size distribution can be determined from the difference in loading between all other two consecutive data points. In light of the underlying assumption of the model regarding saturation conditions it is advised to apply this approach on the desorption branch. The BJH-pore size distribution is limited to pore diameter equal or higher than 3.4 nm (equivalent to $(P/P_0)<0.42$ for nitrogen adsorption at 77K).[10] After the cumulative pore volume (V) and cumulative pore surface area (A) of pores are determined, the average pore

diameter can be calculated according to different pore shape geometry: 2V/A for slit-shaped pores, 4V/A for cylindrical pores, and 6V/A for spherical pores.

4.3.1.4 t-plot[6]

The *t*-method, originally introduced by de Boer,[13] assumes that in a certain relative pressure range, where all micropores are completely filled, but bellow vapor condensation in mesopores, the adsorbed volume can be plotted versus a so called statistical adsorbate thickness determined solely by the relative vapor pressure. Then the adsorption within this pressure region may be described by a linear simple equation. From the slope and Y-intercept both the external surface area (surface area of pores larger than micro-pores) as well as the micropore volume can be estimated. For a uniform and one molecule in depth monolayer, the so-called statistical thickness (t) of adsorbate can be calculated by multiplying the number of monolayers (the ratio of the weight adsorbed to the weight corresponding to the formation of a single and uniform monolayer) by the adsorbate diameter (usually taken in the range of 0.35-0.5 nm). In practice, the statistical thickness, t, is calculated with the help of a thickness equation[6]

(S10) $$t(\text{Å}) = \left[\frac{13.99}{0.0340 - \log(P/P_0)} \right]^{0.5}$$

In this narrow statistical thickness range, roughly corresponds to relative pressures of 0.01-0.65 in all of our carbon samples, the *t*-plot, i.e., the volume of gas adsorbed versus the statistical film thickness for the adsorption of nitrogen, can be linear fitted (in a smaller range of 0.35-0.5 nm) using the slope in order to calculate the external surface area, S_{ext}, according to Equation (S11)

(S11) $$S_{ext} = \frac{V_{liq}}{t} = \frac{V_{ads}(STP) \times 15.47}{t} = slope \times 15.47$$

Where V_{liq} is the adsorbed liquid volume; $V_{liq} = V_{ads}(STP) \times 15.47$ in case of nitrogen adsorption at 77K. For plots, which give rise to a straight line passes through the origin, the surface area calculated from the slope is usually comparable to the surface area determined by the BET analysis. The last is an indication of a non-microporous material. The micropore volume, V_{micro}, can be estimated by the positive Y-intercept, i, according to Equation (S12)

(S12) $$V_{micro} = i \times 0.001547(cm^3)$$

The micropore surface area can be calculated from the following equation

(S13) $$S_{micro} = S_{BET} - S_{ext}$$

4.3.2 Results

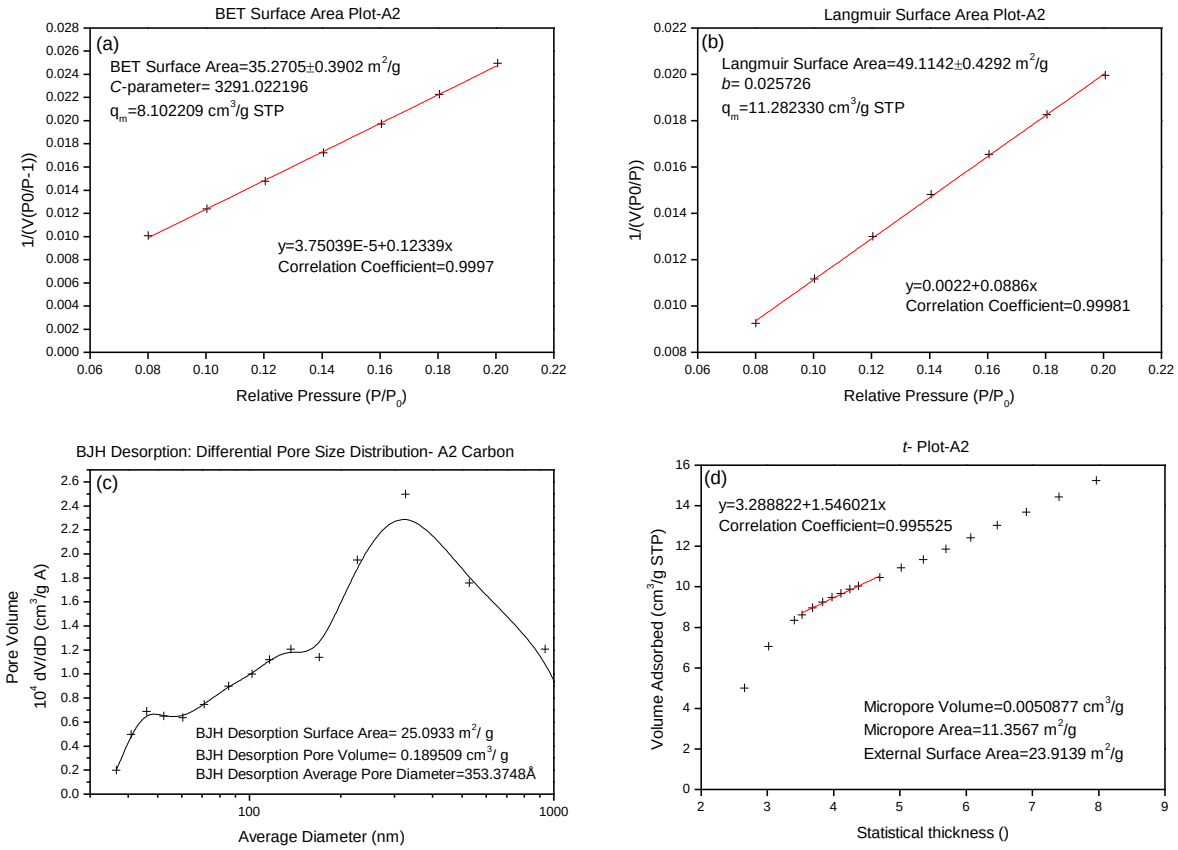

Figure S8. The (a) BET surface area plot, (b) Langmuir surface area plot, (c) BJH pore size distribution, and (d) *t*-plot for A2 air electrode. The main parameters derived from each analysis are written on the plot body.

The BET specific surface area, *C*-parameter and monolayer capacity, q_m, as well as the Langmuir specific surface area of the A2 powder are summarized and presented in **Figure S8**(a) and 4(b), respectively. The data for Langmuir and BET linearized plots was obtained at low relative pressures ranging from 0.08 to 0.2 with a correlation coefficient r^2>0.999. Using Equations(S4) and (S5), the Langmuir and BET specific surface areas were evaluated as 49.11±0.43 and 35.27±0.39 m^2/g, respectively. The

external surface area, micropore volume and micropore surface area obtained from the *t*-plot method were calculated according to Equations (S11), (S12) and (S13) and were found to be 23.91 m^2/g, 0.0051 cm^3/g and 11.36 m^2/g, respectively. Average pore diameter of 35.34 nm based on cylindrical-shaped pores was estimated using BJH method to determine the cumulative pore volume and pore area for mesopores and macropores of width between theses limits, i.e. 1.7-200 nm. Combining the BET, BJH and *t*-plot analysis for the A2 sample reveals that while the total pore volume (0.195 cm^3/g) originate almost solely from mesopores, ~70% of the total surface area (35.27±0.39 m^2/g) originate from mesopores and ~30% from micropores. The analysis of all these quantities allowed for the study of A2 structure. The low surface areas determined by either BET or Langmuir analysis indicated a dramatic decrease in specific surface area due to the addition of the polymeric binder. Although, the highest contribution to the specific surface area originated from mesopores, the contribution from micropores was considerable and should not be underestimated, as illustrated both by the *t*-plot analysis and by BET specific surface area value. The difference between external surface area determined by Equation (S11) and surface area determined by BET analysis gave rise to the surface area origin from micropores. In the case of A2, approximately a third of the surface area determined by the BET analysis is attributed to the presence of micropores, which is also well established by the deviation from linearity appeared in the low relative pressure area in the *t*-plot (**Figure S8**(d)). Still, two thirds of the specific surface area are contributed from pores in the mesoscale. The mesoporous structure is also possibly manifested in the small hysteresis loop observed at high relative pressure (>0.9),[4] where the adsorption isotherm steeply increased at pressure close to the saturation vapor pressure. The BJH pore size distribution (**Figure S8**(c)) reveal that for pores in the mesopore and macropore range (1.7-200 nm), there is a broad distribution of pores revolving around higher values of mesopores (maximum ~30- 40 nm) and around the macropore range (> 50 nm). The broad distribution of pores around 35 nm, were found to be in good agreement with the average pore diameter of 35.34 nm derived from the BJH analysis based on the cylindrical-shape pore model. Although, A2 sample has a relatively small specific surface area, it is still safe to say that the surface area contributed from macropores will be negligible and A2 sample has mostly a meso- and microporous structure, as indicated by the adsorption/desorption isotherm and BET and *t*-plot analysis, their pore size distributions. Returning to the adsorption/desorption isotherm of A2, it is interesting to see some interesting features.

For example, although a mild increase in volume adsorbed is observed at low relative pressures, 30% of its surface area originate from micropores. A deeper look into the *t*-plot analysis reveals that such result can be reconciled with the practically zero micropore volume indicating the presence of micropores on the small micropore scale rather on the higher micropore scale having more micropores with smaller diameter than less micropores with large micropore diameter. The last is highly relevant for battery performance as ca. 30% of the surface area could not be available for discharge products deposition. However, it is also possible that as the rest of the surface area are broadly distributed around higher values of mesopores (maximum ~30- 40 nm) and around the macropore range (> 50 nm), the last is compensated.

4.4 HRSEM Images of Electrodes with different Carbon:Binder:PFCs weight ratio

The effect of PFC addition was clearly observed from electrode A2 with no PFC all through electrode A5 with 35%wt PFC to electrode A6 with no PFC but with 40%wt binder. An accurate comparison was done by comparing A2 to A3 and A3' and A6 to A4, A4' and A5, i.e. comparing between cathodes with the same carbon: fluorinated binder (both PVDF and PFC together). The trends observed in both groups was similar indicating a more "fluffier" surface with higher roughness for all PFC-based samples.

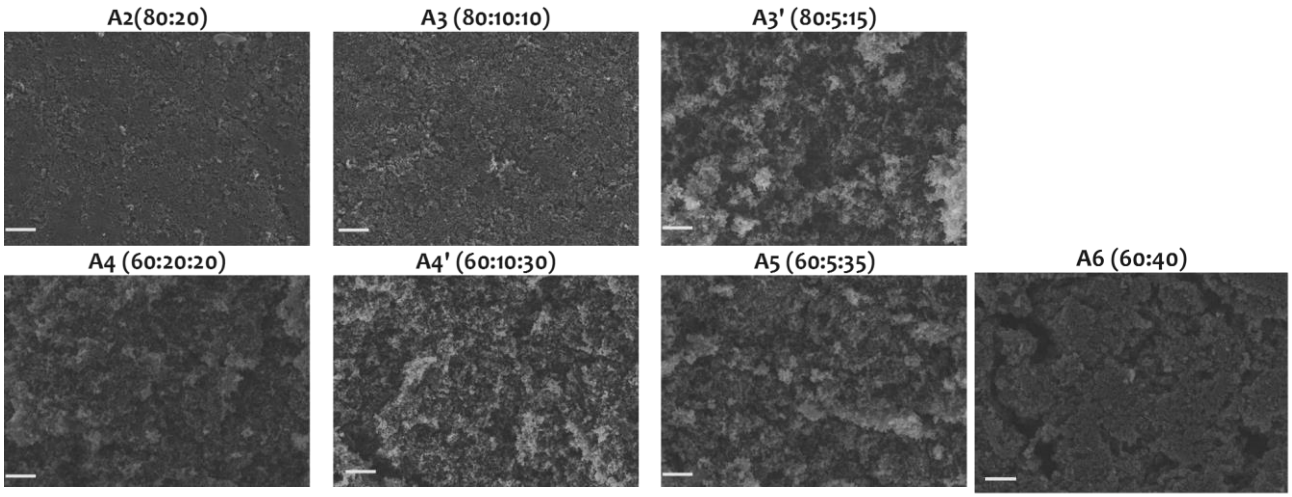

Figure S9. HRSEM images of electrodes prepared with different carbon:binder:PFC weight ratios. Scale bar-1 µm.

4.5 HRSEM Images of A2, A4 and A5 Electrodes Cross-Section

A closer look into the electrode bulk rather than its surface was achieved by both horizontally slicing the electrode in the middle and observing it in the HRSEM and by observing a cross section of the electrode using focus-ion beam (FIB), all presented in **Figure S10** for A2, A4 and A5. The electrodes separated in the middle showed similar morphologies to the one observed on the top view of each electrode, however, no equivocal conclusion can be derived from the cross section images.

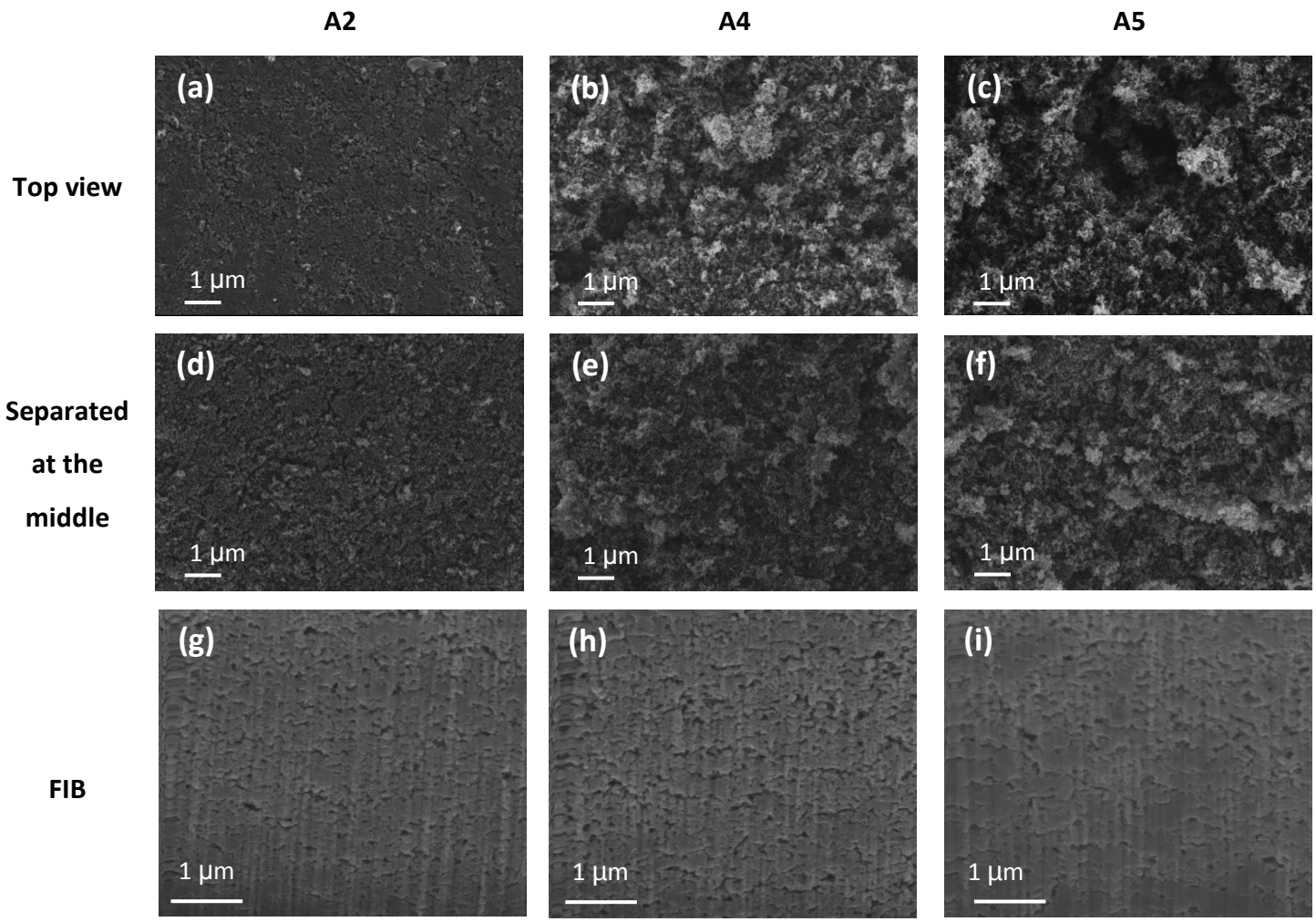

Figure S10. Top view HRSEM images, images taken after electrode was seperated at the middle and FIB images of pristine (a,d,g) A2, (b,e,h) A4 and (c,f, i) A5 air-electrodes, respectively. scale bar- 1µm.

5 Liquid Adsorption Studies

There are numerous adsorption methods available for characterizing porous carbon materials and for the determination of their specific surface area.[14,15] Although, the characterization of porous solids by gas adsorption is highly informative, most surfaces are heterogeneous leading to a non-uniform surface coverage, and in some cases are inapplicable. The pretreatment in gas adsorption techniques, including degassing the sample at relatively high temperature and vacuum conditions, makes such technique inappropriate for specific surface are determination for the A and B-type cathodes as the solid perfluorocarbon can simply evaporate during sample preparation. In such cases, an alternative method based on the adsorption of dyes and other solute molecules

from solution should be considered. The last is usually easy to carry out, but is often difficult to interpret. As it was already demonstrated that the surface area and even the micropore volume and the total pore volume of different carbon types can be estimated by iodine and methylene blue numbers using multiple regression,[16] both iodine and methylene blue adsorption experiments were performed for the specific surface area evaluation of the A and B-type samples.[16–21]

The dimensions of methylene blue (2.08 nm^2)[39,46] allow it to be adsorbed in mesopores and large micropores, while iodine molecules (0.4 nm^2), [39] which possess inferior dimensions, can penetrate pores on the microscale.

5.1 Batch Equilibrium Studies (Methylene Blue)

Methylene blue is a basic aniline dye with the molecular formula $C_{16}H_{18}N_3SCl$ (**Figure S11**). It has many uses as an indicator, and inhibitor, especially in the chemistry, biology and medicine fields and is also used for characterizing the adsorptive nature of different carbons and evaluating their specific surface area.[22,23]

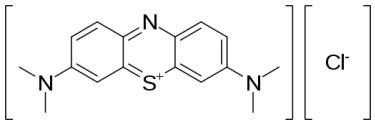

Figure S11. 3, 7-bis (Dimethylamino)-phenothiazin-5-ium chloride also known as Methylene blue.

Adsorption tests were carried out in a set of glass vials (20 ml), where 10 ml of methylene blue (MB) solutions with initial concentration of 50-500 mg/l were place. The pH of MB solution was adjusted to be in the range 6.5–7.5, which is below the pH_{PZC} of the carbons, by adding 0.1M HNO_3 or 0.1M NaOH. Equal mass of 0.01 g of the adsorbent was added to each vial. The vials were capped, rotated at 120 rpm at 22±2 ◦C for 12h and kept for additional 12h at 22±2 ◦C to achieve equilibration. The same procedure was followed for each A-type carbon mixture (**Table 1**) as well as for B1, B2 and B4 samples with activated carbon (PWA, Calgon Carbon Corporation) replacing the originally carbon black (C65, Timcal) used in the A-type samples. Aqueous samples were taken from the solutions for concentration measurements by separating the adsorbent from the MB solution using a filter paper (Whatman, No. 1). The remaining concentration of the MB in the solution after equilibrium adsorption was measured by a double beam UV–Vis spectrophotometer (PerkinElmer, Model

LAMBDA 950 UV/Vis/NIR Spectrophotometer, USA) at 664 nm. The amount of adsorption at equilibrium, q_e (mg/g), was calculated by

$$q_e = \frac{(C_o - C_e)V}{W} \quad \text{(S14)}$$

where C_o (mg/l) is the concentration of the methylene blue solution at starting time (t = 0), C_e (mg/l) is the concentration of the methylene blue solution at equilibrium time V is the volume of the solution (l) and W is the mass of dry adsorbent used (g). Then, the specific surface area $S(m^2 / g_{carbon})$ of the different carbon samples was determined according to the following equation

$$S = \Gamma_m \cdot N_A \cdot \sigma \cdot 10^{-20} \quad \text{(S15)}$$

Here $N_A(molecule/mole)$ is Avogadro's number, $6.023 \cdot 10^{-23}$(molecules/mole), and $\sigma(\text{Å}^2 / molecule)$ is the occupied surface area of one molecule of methylene blue which equals to 197.2 (Å^2/molecule).[24] $\Gamma_m(mole / g_{carbon})$ is number of moles of methylene blue adsorbed per gram sorbent at equilibrium required to form a monolayer and is calculated according to Equation (S16).

$$\Gamma_m = \frac{q_m}{M_W} \cdot 10^{-3} \quad \text{(S16)}$$

$M_W(g/mole)$ is the molecular weight of methylene blue, 373.9 (g/mole) and $q_m(mg / g_{carbon})$ is the amount of methylene blue adsorbed at the monolayer of sorbent. In order to calculate the specific surface area by batch studies and according to Equation (S16), the amount of methylene blue required for a monomolecular coverage, i.e. q_m, must be evaluated. The analysis of the experimental data and its fit to the appropriate isotherm model is an important step towards the determination of the monolayer coverage and finally the specific surface area. The adsorption isotherm, adsorbed distribution between the liquid and solid phase at equilibrium, of A and B-type carbon-based samples were studied by four different isotherm models: Langmuir,[7] Freundlich,[25] Redlich and Peterson[26] and Multilayer[18] (Figure S12).

Isotherm model		Nonlinear form		Linear expression	Plot
Langmuir [36]	(1)	$q_e = \frac{K_L c_e}{1 + a_L c_e}$,	(2)	$\frac{c_e}{q_e} = \frac{1}{K_L} + \frac{a_L}{K_L} c_e$	$\frac{c_e}{q_e}$ versus c_e
Freundlich [37]	(3)	$q_e = K_F \cdot c_e^{n_F}$	(4)	$\log q_e = \log K_F + n_F \cdot \log c_e$.	$\log q_e$ versus $\log\ c_e$.
Redlich and Peterson [38]	(5)	$q_e = \frac{K_R \cdot c_e}{1 + a_R c_e^{b}}$	(6)	$\ln\left(K_R \frac{c_e}{q_e} - 1\right) = b \ln(c_e) + \ln(a_R)$.	$\ln\left(K_R \frac{c_e}{q_e} - 1\right)$ versus $\ln(c_e)$
Multilayer [39]	(7)	$q_e = \frac{Q_m K_1 c_e}{(1 - K_2 c_e)[1 + (K_1 - K_2) c_e]}$,	(8)	Second-order polynomial form $\frac{c_e}{q_e} = \frac{c_e^2 (K_2^2 - K_1 K_2) + c_e (K_1 - 2K_2) + 1}{Q_m K_1}$	$\frac{c_e}{q_e}$ versus c_e
Fritz and Schluender [40]	(9)	$q_e = \frac{A \cdot c_e^{\alpha}}{1 + B \cdot c_e^{\beta}}$		—	—

Figure S12. Mathematical equations of the applied single component isotherm models.[27]

Among the four mentioned models, the Redlich and Peterson isotherm and multilayer isotherm models were found to best fit the experimental data and thus their calculation process will be described to greater details. The Redlich and Peterson isotherm combines both Langmuir and Freundlich models, thus the adsorption does not follow an ideal monolayer adsorption model and can describe both homogeneous and heterogeneous systems. As the model has three unknown empirical parameters, we were not able to plot the linear form of Redlich and Peterson's equation. Therefore, a minimizing procedure was adopted[14,28] to solve the linear equation by maximizing the correlation coefficient between the theoretical model prediction (q_e) and experimental data with solver add-in function of the Microsoft excel. The multilayer physisorption isotherm, also known as the Brunauer, Emmet, and Teller (BET) isotherm is a theoretical equation already described in previous section (Section *4.3.1.2*) developed to derive multilayer adsorption systems with a monolayer coverage lying between 0.5 to 1.5.[14] This adsorption consists of an initial first layer adsorption followed by multilayer attachment onto previous layers.[18] The values of the model parameters for the multilayer model were determined through the second order polynomial form according to the equation presented in **Figure S12**. The applicability of each model was determined by comparing the correlation factor R^2.

5.2 Iodine Number

Iodine number is defined as the gr of iodine that is consumed by a 100 gr of a chemical substance. Iodine number is a fundamental parameter used to characterize activated carbon adsorption performance and is commonly used to roughly estimate the surface area of activated carbons. It was established that, due to its size, the iodine mostly

adsorbed to micro and mesopore, thus higher degree of iodine adsorption corresponds well with the specific area for porous carbon with micro and meso-porous structure.[19] Saying that, in high surface area carbon (>1000 m^2/gr) the iodine adsorption activity proved to be lower due to pores with sizes smaller than 1 nm as the iodine molecules cannot penetrate such small pores.[19] It was established that the iodine number corresponds well with the specific surface area, determined by nitrogen,[19] and that higher degrees of iodine adsorption have been reported to indicate a higher surface area and the presence of largely micro and mesoporous structures. [19]

The iodine number (mg/g of carbon) for different A-type cathode was evaluated using the procedure proposed by the Standard Test Method (ASTM D 4607- 86). The A-type samples (approximately 1 g) were placed in a 250 ml dry beaker, and were treated with 10 ml 5%HCl until each sample was fully wetted. Then 100 ml of iodine solution (2.7 g of Iodine (Merck) and 4.1 g of potassium iodide (Merck) in 1 L of de-ionized water, 0.1 M) was poured into the beaker, and the mixture was vigorously shaken for 30 s. The resulting solution was filtered and 50 ml of the filtrate was titrated with sodium thiosulfate, $Na_2S_2O_3$, (0.1 M) until the solution became colorless, using 1 ml of starch (1 g/l) as indicator close to the end point where the solution is pale yellow. A blank was prepared without adding carbon. The percent iodine removed by each carbon was calculated according to Equation (S17): [17]

$$\frac{Na_2S_2O_3[blank](ml) - Na_2S_2O_3[sample](ml)}{Na_2S_2O_3[blank](ml)} \quad \text{(S17)}$$

The iodine amount adsorbed per gram of carbon (X/M) was calculated according to the following equation:

$$X/M = \{(N_1 \text{ x } 126.93 \text{ x } V_1) - [(V_1 + V_{HCl})/V_F] \text{ x } (N_{Na2S2O3} \text{ x } 126.93) \text{ x } V_{Na2S2O3}\}/M_c \quad \text{(S18)}$$

where N_1 is the iodine solution normality, V_I is the added volume of iodine solution, V_{HCl} is the added volume of 5% HCl, V_F is the filtrate volume used in titration, $N_{Na2S2O3}$ is the sodium thiosulfate solution normality, $V_{Na2S2O3}$ is the consumed volume of sodium thiosulfate solution and M_C is the mass of activated carbon.[16]

5.3 Surface Area Considerations

According to Equation S15 and assuming the changes in iodine adsorption is proportional to the micropore surface area, the external surface area can be predicted to increase as well with the increase in PFC additive, according to the following

consideration and assuming the total surface area is smaller than $(b-1)/(a-1)$ times the micropore surface area,

$$S_{ext} = S_{BET} - S_{micro}$$
$$S'_{ext} = aS_{BET} - bS_{micro}$$
$$S'_{ext} \overset{?}{>} S_{ext};\ a<1,\ b<1$$
$$aS_{BET} - bS_{micro} > S_{BET} - S_{micro}$$
$$\frac{S_{BET}}{S_{micro}} < \frac{b-1}{a-1}$$

Thus, for example for samples A2 and A4 the ~74% decrease in iodine adsorption (i.e. 1-*b*) and ~19% decrease in total surface area (i.e. 1-*a*), under the assumption that the total surface area is larger ~4 times than the micropore surface area, will lead to an increase in A4 external surface area, which is attributed to the most relevant pore size for Li-O_2, the mesopores. Not only that, the more difference between the total surface area and the micropore surface area, the greater the increase in external surface area moving from sample A1 to A4.

6 B-type electrodes

Three different samples were investigated all with pulverized activated carbon: B1, B2 and B4. The B-type samples consisted of activated-carbon (PWA, Calgon Carbon Corporation), PVDF binder and solid state PFC in a weight ratio of 100:0:0, 80:20:0 and 60:20:20 for B1, B2 and B4, respectively, in accordance with A1, A2 and A4 samples. Both A- and B-type samples differed from one another only in the type of carbon used. The carbon in B-type samples was pulverized activated carbon with a BET surface area of 900-1000 m^2/g as declared by its manufacture. The specific surface area (m^2/g) of samples B1, B2 and B4, determined by methylene blue adsorption and analyzed according to the best-fitted adsorption model, i.e. multilayer, and the iodine number (mg/g_{sample}), are presented in **Figure S13**.

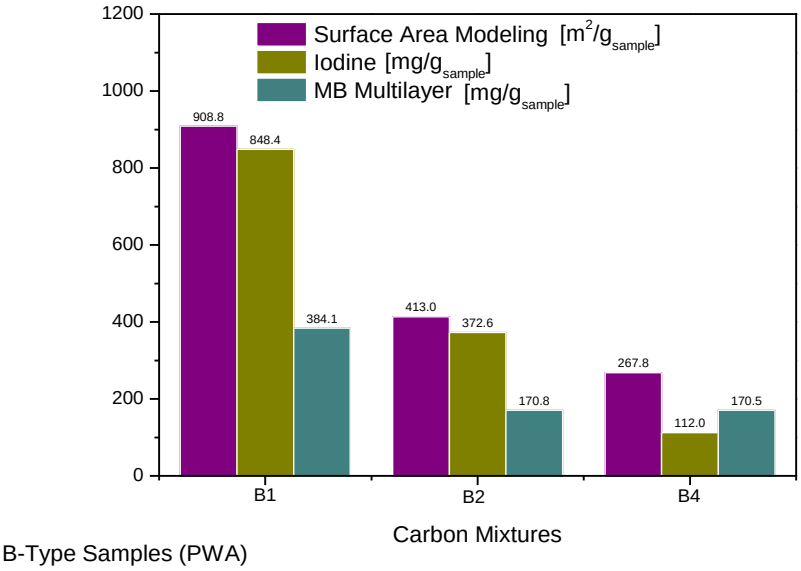

Figure S13. The surface area modeling (m^2/g_{sample}) (purple), according to the mathematical model presented in [16] based on iodine number (mg/g_{sample}) (dark yellow) and methylene blue number (mg/g_{sample}) (dark cyan), for B1, B2 and B4 . All values are normalized to the sample weight.

The total surface area was determined according to the mathematical model[16] already presented for A-type cathodes and the results for B-type cathodes are presented in **Figure S13**. The specific surface area for the pristine carbon (sample B1) lays in the range defined by the manufacture. The specific surface area seems to correlate well with the iodine adsorption both in B1 and B2 samples which is expected for activated carbon, as its surface area is largely determined by its micropore volume. In sample B4 the iodine number decreased drastically compared to B2 sample as oppose to methylene blue number which remained the same. It appeared as the addition of polymer binder decreased the surface area drastically in activated carbon samples due to pore clogging of both micro and meso-pores. The addition of PFC (sample B4) decreased the surface area by almost 50% compared to sample only having PVDF (sample B2), which was solely due to micropore clogging as the methylene blue remained unchanged. Thus, it can be predicted that if PFC addition only decrease pores on the microscale, which is practically transparent to discharge products, but did not alter the mesopore structure, no drastic change in Li-O_2 battery performance is expected. Further strengthening to negligible structural changes on meso-pore scale was accomplished with HRSEM images of both B2 and B4 electrodes (**Figure S14**). The advantageous morphological and structural changes observed upon PFC addition to A-type sample, did not appear

in B-type sample. The bigger particle size compared to carbon black made activated carbon samples, i.e. B-type samples, less flexible to structural changes, thus the addition of PFC did not able structural changes, less evenly distributed on carbon surface (**Figure S14**(d)) and impaired the electrode surface by blocking micro-scale pores.

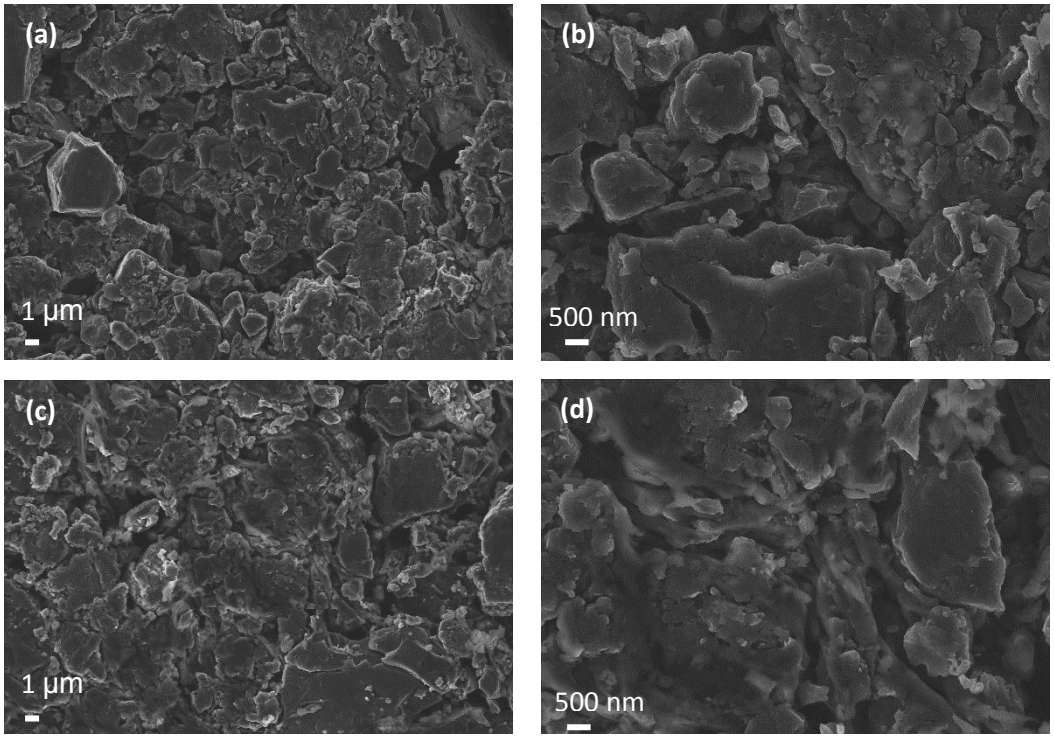

Figure S14. HRSEM images of (a, b) B2 and (c,d) B4 samples.

7 Static Contact angle determination via Compact Powder Method

The wettability assessment of different carbon powders was determined using the powder compact method.[29,30] After grinding different carbon samples (**Table 1**) into a fine powder andpreparing pellets exerting a constant pressure, the contact angle was measured using the sessile drop method. The direct contact angle measurements were conducted on the different carbon samples with both deionized water and triglyme as the wetting liquid. The contact angles were measured on as-prepared pellets ("dry") and wetting-liquids pre-soaked pellets. The last is a common method to avoid possible errors due to wetting-liquid penetration.[29] Although the pellets were pre-loaded with triglyme, the solvent was still consumed by or adsorbed into the sample making it impossible to determine the contact angle. When water was used as the wetting-liquid on both the dry and pre-saturated pellets, the contact angle was stable over time and the

results for both the direct measured and the corrected contact angle according to the compact pellet method, are presented in **Table S1**. Although the contact angle determined via the compact pellet method is sometimes regarded problematic for wettability behavior analysis and may lead to irrelevance of the absolute values especially when compared with other reported values or between two different methods, but are still a good indication of the observed trends.[31]

Table S1. The measured porosity, measured contact angle (θ) via direct method on dry and deionized H_2O pre-saturated pellets and the corrected contact angle (θ*) for the pre-saturated pellets according to references [29,30] are presented for A2-A6 carbon samples. Wetting liquid was deionized water.

	Porosity	Measured θ (°)		Corrected θ*(°)
		Dry	H_2O pre-saturated	
A1	-	-	-	-
A2	67.3±1.2	135.1±2.0	119.3±6.3	72.5
A3	54.5±3.0	159.2±4.9	145.2±5.8	72.9
A4	43.2±8.2	154.7±4.0	113.4±4.5	71.6
A5	54.4±5.9	156.7±3.8	129.7±3.6	71.1
A6	40.3±3.8	128.4±0.8	120.6±5.5	64.6

Although the H_2O-liquid drop was stable for at least 30 minutes the contact angle measured for the dry and pre-soaked pellets showed a great variation for the different carbon samples and so, the corrected contact angles, which are the contact angles calculated according to reference [32] were calculated only for the pre-saturated pellets. Let us compare the results of samples with different weight percentage of carbon, i.e. A2 and A3 (80%wt carbon) as oppose to A4 and A5 (60%wt carbon). It was hypothesized that increasing the percentage weight amount of fluorinated material (PVDF and solid PFC) on the expense of carbon will increase the contact angle of water as fluorinated material are tend to be more hydrophobic than most carbon blacks. However, the results presented in **Table S1** reveal that hardly any change was observed for the corrected contact angle calculated for samples A2, A3, A4 and A5. To explain such result, it is important to pin point the main differences between PVDF and solid PFC. While PVDF is a solid macromolecule with the following repeating unit -[CH_2-CF_2]-, solid PFC is a "wax" like material with significantly lower molecular weight,

which can be easily homogeneously dispersed in the carbon sample without drastically affecting the microstructure of the carbon particle size and distribution, which can further affect the wettability behavior. The PVDF is the main material "gluing" the particle size and preventing their crumbling down (as was observed when A1 pellets were tried to be made). Thus, a more correct way of analyzing the results will be to redefine the relative amount of carbon and PVDF in samples A2, A3, A4 and A5 as they were made from only the two components. Such an approach reveal that the relative amount between the carbon and PVDF ranges between 80:20 to 92:8 for samples A2 and A5, respectively. Thus, in such samples where the relative amount of carbon and binder remained practically the same, the contact angle of water measured was practically the same in all samples. Now, let us compare sample A2 and A6 which differ significantly in the relative amount and PVDF. Again, the higher amount of PVDF should have potentially increase the contact angle of water as the fluorinated binder is hydrophobic (θ=89º, at smooth surfaces). However, the contact angle decreased by approximately 8º. In the range of experimental error as well as higher surface roughness observe for A6 pellet it is possible that all of the above caused the observed discrepancies in contact angle measurement.

8 Sieved vs. not sieved A-type carbon samples

The preparation of air electrodes for Li-O_2 battery from A-type carbon sample included only the grinding of the samples into fine powders in order to ease the compression of the powders into an air-electrode. The sieving of powders was introduced only in the Washburn capillary rise experiments and compact pellet method in order to minimize possible errors originate from different particles size and particle size distribution of the powders as noticeable difference in powders size were observed for different weight ratios of carbon versus PVDF and solid PFC, which can further affect the wettability of carbons samples as larger particle size distribution often increase the penetration rate.[33] However, it was reported that the advancing contact angle obtained from WCR for powder materials were found to be overestimated and more reasonable values were resulted when relatively large powders (500-2000 um) were used to pack the tubes.[34] In order to get a deeper insight into the carbon mixture used to produce air cathodes for Li-O_2 batteries, all A-type carbon samples were treated in the same manner as they are treated prior to the air electrode preparation, which mean they were prepared according to the experimental section but were only vigorously stirred for 24 hours without the

last stage of sieving added when the samples were characterized by capillary rise experiments and contact angle experiments via the compact pellet method. It is important to note that the difference in the powders particle were noticeable by eye before and after the last stage of sieving. The liquid penetration velocities of triglyme in A1, A2 and A4 sieved and stirred samples are presented in **Figure S15** and reveal that the liquid penetration rate is not dramatically affected by the last process of sieving and all results produced and presented are a good indication of the real processes occur when the powder is only stirred and pressed into an electrode as a part of the Li-O_2 cell. In addition, the results presented in **Figure S15** indicate that the wetting process in the carbon cathodes prepared from carbon black with a primary particle size of ~40 nm is influenced by the relative amount of the carbon compared to the added fluorinated material and less by the macrostructure of the samples. It is possible that the last conclusion is correct only when low surface tension liquids are used and will not occur with liquids showing bad wetting behavior.

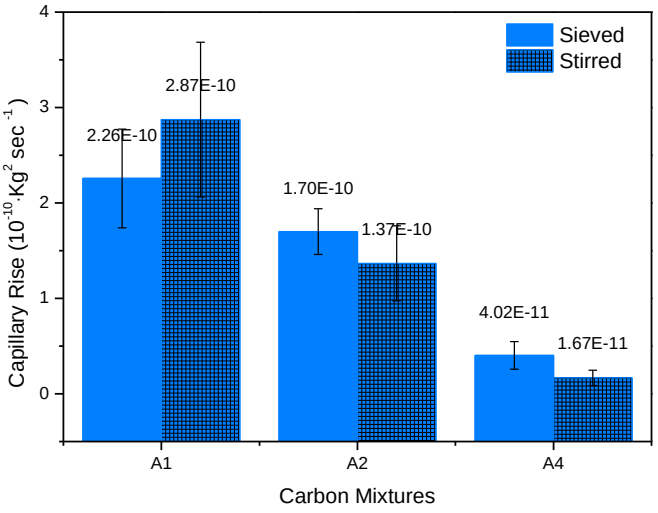

Figure S15. Triglyme penetration rate obtained by Washburn capillary rise method using capillaries after carbon powder samples were only stirred into a fine powder without further sieving the samples.

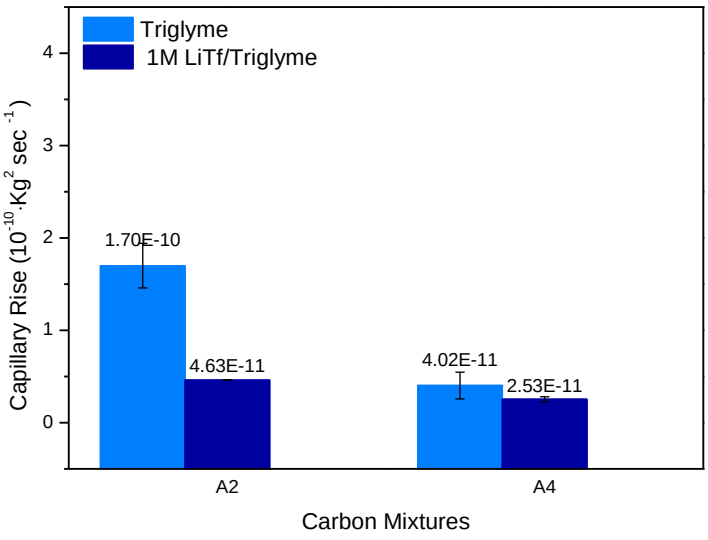

Figure S16. Triglyme and 1M LiTf/Triglyme penetration rates obtained by Washburn capillary rise method using capillaries with 0-150 µm carbon powder samples.

When exploring the wettability of solvents on different carbon powders with respect to Li-O_2 battery, it is important to transfer to the specific electrolyte system found in common Li-O_2 battery system, i.e. 1M LiTf/triglyme. The addition of inorganic salts to aqueous solutions have been widely investigated for over a century ago indicating higher surface tension in salted solutions compared to pure water.[35] However, in our system the dielectric constant of triglyme and air do not differ significantly (7.5 vs. 1, respectively), thus the depletion of solute near the liquid-air interface, i.e. the change of electrolyte density near the interface is not predicted to occur in a large extent, predictably leading to only a small increase if any in the surface tension of the salted-organic solvent.[36] as oppose to aqueous based systems, where the presence of a salt can invoke an electrostatic image force by ions near the air-liquid interface due to the large difference between the dielectric constant of water versus air leading to an increase in the surface tension.[37] Although the surface tension with and without the addition of lithium salt is not predicted to change drastically, the wetting behavior of such solvents depends not only on the liquid on hand but on the surface as well. Thus, it is interesting to explore the wetting behavior of lithium-based electrolytes in both A2 and A4 carbon samples, which are the two powders showing the most promising Li-O_2 battery performance.

Table S2. Surface tension of different liquids: deionized water, triglyme and 1M LiTf/Triglyme determined by the pendant drop method at 24ºc.

	γ_{LV} [mN m^{-1}]
H_2O	77.5±0.3
Triglyme	38.6±0.1
1M LiTf/triglyme	40.8±0.3

Figure S16 shows the penetration rates of triglyme and 1M LiTf/triglyme obtained for sieved A2 and A4 carbon samples and **Table S2** summarizes the surface tension of different solvents measured via the pendant drop method. As expected, no vast difference was observed for the surface tension of triglyme and 1M LiTf/triglyme, but as the penetration process is more complex, differences in the penetration rates were observed between the pristine organic solvent and the salted solvent (**Figure S16**). Although, the penetration rate of triglyme decreased by 75% in A4 sample compared to A2, a smaller change was observed when lithium salt was added to the organic solvent. Leading the penetration rate of 1M LiTf/triglyme to be only twice as high in A2 compared to A4 carbon sample. Although the wetting behavior of 1M LiTf/triglyme decreased when transferring from A2 to A4 carbon sample, it is still in the same order of magnitude. It is important to note that the conclusions made with respect to wettability of electrolyte in A2 and A4 samples should be considered carefully. Although the wetting liquid remained the same, the carbon matrix was changed and according to the Washburn capillary equation presented in references [30,34], the change in penetration rate could result from the C parameter, which is a structure characteristics, rather than from the dynamic contact angle, which mirrors the wettability behavior.

9 Washburn Capillary Rise Method-Results for A2 and A4 electrodes

Regardless of the complicated nature of the penetration process, the liquid penetration velocity ($Kg^2 \cdot sec^{-1}$) of the wetting liquid in A2 and A4 carbon mixtures were determined from the linear part of m^2 (Kg^2) versus t (sec) plot, as illustrated in **Figure S17**, and was found to be four times higher in A2 compared to A4 sample.

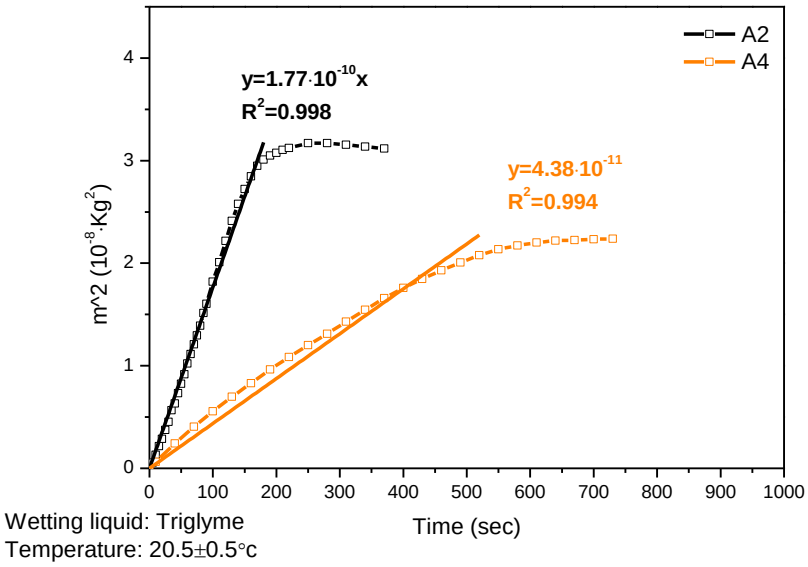

Figure S17. Triglyme penetration rate obtained by Washburn capillary rise method using tubes with 0-150 µm carbon powder samples. t=o corresponds to penetration of the wetting liquid into the carbon-based sample and not to the moment of column submersion in the wetting liquid.

Both A2 and A4 penetration rate curves can be divided into two main stages: penetration (stage I) and saturation (stage II). In stage I, the liquid weight increases gradually at a constant rate until it reaches a constant value, whereas in stage II, the liquid mass does not change due to its saturation in the carbon sample. While the penetration rate is an important parameter, the shape of the curve and the transition from stage I to stage II can provide a useful insight into both carbon mixtures that differentiate from one another by the presence of the solid-state perfluorocarbon. In the case of carbon mixture A2 (**Figure S17**, black curve), the shorter and clearer transition from the stage I to stage II compared to A4 may be indicative of a more even liquid penetration which may result from larger particle size distribution, even spaces between carbon particles and thus similar rates of liquid capillary penetration. For sample A4 (**Figure S17**, orange curve), the transition between stage I and II is more gentle, gradual and longer. Two major causes can be responsible for such a different liquid penetration behavior: The agglomerates size distribution and surface chemistry. Although, both samples were put through a 150 µm sieve the agglomerate size distribution remains unknown and can alter the penetration behavior so larger particles/agglomerates and smaller agglomerates size distribution can create some diversified capillaries leading to a larger time difference between flow (stage I) and saturation (stage II) as observed for

sample A4. As also supported by Nishi *et al.*[20] Showing an indistinct and a less sharp stage I-II transition for less homogeneous carbon-based samples with smaller bulk density.

10 Relative surface area and wettability behavior

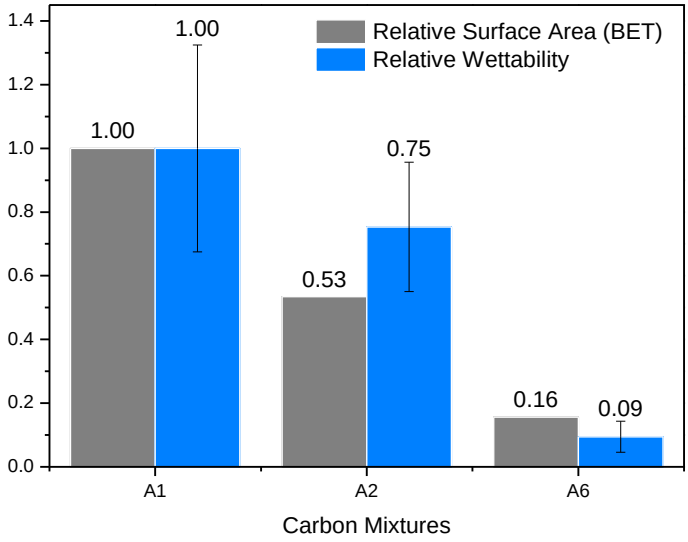

Figure S18. The BET surface area (grey) and the penetration rate of triglyme in A1, A2 and A6 relative to the penetration velocity and BET of A1, respectively.